

Supporting Information for:

Size and Elemental Distributions of Nano- to Micro- Particulates in the Geochemically-stratified Great Salt Lake

Ximena Diaz^{†,§}, William P. Johnson^{†,}, Diego Fernandez[†], David L. Naftz^{‡,†}*

[†]Department of Geology & Geophysics, University of Utah, 135 S 1460 E Salt Lake
City, UT 84112; [‡]U.S. Geological Survey, 2329 West Orton Circle, Salt Lake City, UT

84119

* Corresponding author e-mail: william.johnson@utah.edu; phone: (801)581-5033; fax: (801) 581-7065.

[§] Current address: Department of Extractive Metallurgy, Escuela Politécnica Nacional, Quito – Ecuador.

Water samples. Water samples for total and dissolved major and trace element analysis were collected in acid-rinsed polyethylene bottles from four stations (2267, 2565, 2767 and 3510, [Figure 3 in the text](#)) at the Great Salt Lake (GSL). At two stations (2267 and 2767), samples were collected from two depths representing the shallow brine layer. At the remaining two stations (2565 and 3510), samples were collected from three or four depths representing the shallow and deep brine layers and the interface between them (0.2, 3, 8, and 6.5 m, respectively).

Five samples (250 mL) were collected from each location using a peristaltic pump with acid-rinsed C-flex tubing (Cole-Parmer's Masterflex, Vernon Hills, IL). Two of the five samples were filtered (0.45 μm pore size, capsule-type filter). Four replicates (2 filtered and 2 raw) were acidified (trace metals grade nitric acid, 2 mL, 7.7 N); one replicate was kept unacidified (raw unacidified, RU). All five replicates were stored on ice until to be transferred to a refrigerator. One each of the filtered-acidified and raw-acidified samples were sent to a contract lab (Frontier Geoscience, Seattle, WA) for total Se analysis. The other replicates were stored at 4°C. The acidified replicates (filter and raw) were analyzed for major and trace elements (Al, As, Ba, Ca, Cd, Co, Cu, Fe, K, Li, Mg, Mn, Mo, Na, Ni, Pb, S, Sb, Se, Ti, U, V, Zn) via collision cell inductively-coupled plasma mass spectrometry (CC-ICP-MS) at the University of Utah. The raw unacidified replicate was used for particulate fractionation analysis via asymmetric flow field flow fractionation (AF4) coupled with the CC-ICP-MS at the University of Utah.

At the remaining two stations (2565 and 3510), samples were collected from three or four depths representing the shallow and deep brine layers and the interface between them (0.2, 3, 8, and 6.5 m, respectively).

Aqueous characteristics of shallow and deep brines included temperature, conductivity, pH, oxidation-reduction potential (ORP), density, salinity and dissolved oxygen (DO), were measured using a Hydrolab Troll 9000 (In-Situ Inc., Fort Collins, CO). The major changes in water chemistry coincided with transition to the deep brine layer, about 6.5 m depth below surface, where dissolved oxygen (DO), oxidation-reduction potential (ORP) and pH decreased and conductivity increased (Figure 1 in the text). Temperature profile (Figure 2 in the text) demonstrated that the deep brine layer is insulated and showed lesser temperature variation relative to shallow brine layer, resulting in the deep brine layer being cooler than the shallow brine during summer, and warmer than the shallow brine in winter.

Average total concentrations for trace metals analyzed in 66 raw acidified (RA) and 66 filtered acidified (FA) samples showed trends with depth (0.2 m, 3.3 m, 6.5 m and 8.0 m) that differed among the elements (Figure S1). The samples were taken from locations spread across the south arm of the Great Salt Lake, and showed consistent values that allowed their averaging despite significant spatial distances between samples as shown in the error bars (Figure S1).

Al, Mn, Fe, Ni and Pb showed increased concentration in the deep brine layer (below 6.5 m and 8.0 m depths) relative to the shallow brine layer (Figure S1 top) for the RA samples. In contrast, Co, Cu, As and Ba showed equivalent concentrations in the shallow brine layer and the upper portion of the deep brine layer; whereas their concentrations increased significantly (from 19 to 79%) at the bottom of the deep brine layer (about 8.0 m below the lake surface). Mo, Sb, U and Se showed similar concentrations at all depths (Figure S1 top).

In the FA samples Al and Mn showed increased concentration in the deep brine layer (below 6.5 m and 8.0 m depths) relative to the shallow brine layer (Figure S1 bottom), whereas the majority of the elements showed similar concentrations at all depths, except Ni, Cu and Pb that showed larger concentrations near surface. Fe and Co showed lower concentrations in the intermediate depths (3.3 and 6.5 m) (Figure S1 bottom).

Fractionation. The dimensions of the asymmetric flow field-flow fractionation (AF4) channel used were 27.3 cm in length, 224 μm in thickness and a channel volume of 0.71 mL, calculated according to Litzén (1993). The membrane used in the channel was a 10K Da regenerated cellulose. The Postnova AF4 equipment automatically controls the different outflow rates (to the detector, the cross flow and to the slot pump). However, the use of a 1kDa membrane produced outflow rates that could not be precisely controlled by the equipment. Therefore we used a 10kDa membrane in the AF4 channel.

The AF4 was connected to three detectors (UV absorbance, fluorescence and CC-ICP-MS) in serie, via a 0.25-mm i.d. peek tubing. Anoxic samples (samples from the deep brine layer) were kept in the AF4-CC-ICP-MS under anoxic conditions by degassing the carrier with nitrogen prior to use. Great Salt Lake water samples were filtered immediately before to inject into the AF4-CC-ICP-MS system, using a 0.45 μm syringe filter (Nalgene* Syringe Filters, surfactant-free cellulose acetate (SFCA)), for both nanosize ranges (0.5 to 7.5 nm; and, 10 to 250 nm). The CC-ICP-MS removes interferences during detection by the attenuation of polyatomic ions of same mass (but different cross sectional area) as the analyte via counter-current flow of He or H₂ gas immediately upstream of the mass spectrometer. Separate runs using helium and

hydrogen gases in the collision cell (to reduce polyatomic interferences) were used with each sample.

The AF4 was calibrated using standard nanoparticles. Colloidal gold and fluorescent latex beads with known sizes (10, 98 and 200 nm) were used to determine the operation conditions for the nanoparticles range between 10 to 250 nm (Table 1 in the text, Figure S2). For nanoparticles separation in this size range, the AF4 was programmed to use three different cross-flows during the elution to improve the particle separation and the intensity of the UV signal. The calibration curve to convert the retention time in particle size (hydrodynamic diameter) is shown in Figure S2. The calibration curve included the injection, transition and elution times.

Polystyrene sulfonate standards (PSS) with known molecular weights (8K, 18K, 35K and 100K Da) were used to optimize the operation conditions to separate nanoparticles between 0.9 to 7.5 nm in the AF4 (Table 2 in the text, Figure S3). A four-step program varying the cross-flow in the AF4 was used during the elution, which improved the particle separation and the intensity of the UV signal. To convert the retention time in particle size the following expression derived from Prestel et al. (2005) was used:

$$\log d_h = 0.6685 \log MW - 2.6517$$

where d_h is the hydrodynamic diameter (in nm) and MW is the molecular weight (in Da). The calibration curve obtained (Figure S3) included the injection, transition and elution times and the variation of the cross flow during the run. The operation conditions for the CC-ICP-MS are presented in Table S1.

Interestingly, the 8kDa standard showed a very strong signal even though the membrane pore size was 10kDa. This may be due to a formation of an electric double layer on the

membrane (regenerated cellulose) that would be expected to extend 10s of nm into solution, effectively decreasing the pore size of the membrane for PSS.

The AF4 fractionation may produce losses of standards due to the operation conditions (e.g., high cross flow or cross flow changes during the run (Ratanathanawongs-Williams & Giddings, 2000)); concentration of standards (e.g., overloading effects (Bolea et al., 2006)); characteristics of membrane and analyte (e.g., absorption of the analyte to the membrane (Bolea et al., 2006)). The material lost, that did not pass through the membrane, may be eluted prior to the sample, or following cessation of cross flow if the sample is held in place by cross flow. It has been suggested that the higher the cross flow the higher the losses (Ratanathanawongs-Williams & Giddings, 2000). To account for losses in a mixture of different-sized standards with variable cross flow is extremely difficult (Ratanathanawongs-Williams & Giddings, 2000) and was not attempted in this work.

The CC-ICP-MS removes interferences during detection by the attenuation of polyatomic ions of same mass (but different cross sectional area) as the analyte via counter-current flow of He or H₂ gas immediately upstream of the mass spectrometer. Separate runs using helium and hydrogen gases in the collision cell (to reduce polyatomic interferences) were examined for each sample.

Fractionation of GSL synthetic and milli-Q water. A synthetic solution contained the major salts (Cl⁻, Na⁺, Mg²⁺, SO₄²⁻, K⁺, Ca²⁺) that compose the shallow water of the GSL (Table S2).

Results obtained in the GSL synthetic and in the milli-Q water fractionation for the 10 to 250 nm size range (Figure S4b) showed a void peak, which apparently seems to be an

AF4 artifact due to changes in pressure under the operational conditions used in this size range. Not void peak was observed for the GSL synthetic or in the milli-Q water in the 0.9 to 7.5 nm size range (Figure S5b). Only one of the elements analyzed (Mn) in the GSL synthetic solution showed a peak in the 0.9 – 7.5 nm size range similar to that obtained in GSL water samples (Figure S5b), that could be due to contamination in the salts used in the synthetic solution (Table S2).

PHREEQC Modeling of Water Samples. The U.S. Geological Survey (USGS) PHREEQCI software (version 2.14.3, 2007, [://wwwbrr.cr.usgs.gov/projects/GWC_coupled/phreeqc/](http://wwwbrr.cr.usgs.gov/projects/GWC_coupled/phreeqc/)) was used to identify the possible mineral phases present in raw acidified (RA) samples. Average concentrations (Table S3) from multielement analysis of GSL water samples (RA) were used in the modeling. The thermodynamic parameters used are defined in the minteq.v4 database, which is an option incorporated to the program (Parkhurst and Appelo, 1999). The minteq database has thermodynamic parameters for all major and trace metals analyzed in this study. One important limitation of the PHREEQC is that the software uses Debye Hückel expressions to account for the nonideality of aqueous solutions (Drever, 2002; Appelo and Postman, 2005). Those expressions are suitable for low ionic strength but may not be appropriate at higher ionic strengths (Drever, 2002) like for the hypersaline water of the GSL. The latest version of the software has incorporated Pitzer activity coefficients for major elements (e.g., Ba, Ca, Cl, Fe, K, Mg, Mn, Na, S) but not for trace elements, which made ineffective for our purposes that database.

For the simulation, two extreme conditions of temperature observed in the shallow and deep brine layers (2°C and 30°C for the shallow brine and 13°C and 20°C for the deep

brine) were used, to look for seasonal variability. Average values of densities measured in the field (1.11 g/mL for the shallow brine and 1.16 g/mL for the deep brine) were utilized. An average value of ORP (in mV) measured in the field were converted in pe for each brine layer using the equation (Fengxiang and Banin, 1997):

$$pe = \text{ORP(mV)}/59.64$$

The pe values used for modeling were 3.4 for the shallow brine and -5 for the deep brine.

PHREEQC simulations were conducted to examine the mineralogical phases that were supersaturated in both layers. These simulations are only approximate because the PHREEQC software cannot correct the activity coefficients for the hypersaline environment of the GSL.

In oxic brines PHREEQC predicted that the shallow brine is super-saturated with silicates (clays), oxides and oxy-hydroxides of Fe and Al (Table S4 and Figure S6 top). Elements such as Cu, Co and Mg were predicted to form complex compounds with Fe oxide. Three U oxides were also predicted.

PHREEQC simulations for deep brine samples predicted that the majority of trace metals precipitate as sulfides and selenides (Table S5 and Figure S6 bottom). The model also predicted silicates (clays), Al oxy-hydroxides as well as uraninite (UO_2) as stable solid phases in the deep brine layer. Notably, there is one Fe-Al compound (FeAl_2O_4 , Hercynite) that was predicted for both brines (Tables S4, S5 and Figure S6).

The saturation indices (SI) were strongly dependent upon temperature, which ranges from approximately 2°C to 30°C in the shallow brine layer of the Great Salt Lake (Table S4).

SI decreased with increased temperature around 61% (average within a range from 28% to 96% among the compounds) for the Al oxy-hydroxides, such that Al oxyhydroxides became undersaturated at the higher temperature. The opposite trend occurred for the Fe oxy-hydroxides, which increased around 65% (average within a range from 33% to 95% among the compounds) in response to increased temperature in the observed range, showing that Fe oxy-hydroxides are more stable at higher temperature in shallow brines.

The narrower temperature range in the deep brine, from approximately 13°C to 20°C, yield a much reduced range in SI values in the deep brine relative to the shallow brine layer. In general, the compounds predicted for the deep brine layer became less supersaturated at higher temperature (Table S5).

Settling velocity in the water column of the Great Salt Lake. The approximate settling velocity for equivalent spherical particles can be calculated by the Stoke's equation as follows:

$$V_s = \frac{(\rho_s - \rho_f)gd^2}{18\mu}$$

where V_s is the terminal velocity (in cm/s); ρ_s and ρ_f are the densities (in g/cm³) for the solid and the fluid, respectively; g is the gravity constant (in cm/s²); μ is the viscosity (in g/cm s); and, d is the particle diameter (in cm). For nanoparticles smaller than 100 nm, electrostatic interactions and Brownian motion reduce the settling velocity virtually to zero, especially for clays because of their aspect ratio. Stoke's formula used here may overestimate the settling velocity of nanoparticles larger than 100 nm, but was used for

comparison. Nanoparticles are commonly defined as particulate matter with at least one dimension that is less than 100 nm (Christian et al. 2008).

A representative density is provided by boehmite (γ -AlOOH) nanoparticles ($\rho_s = 3.04$ g/cm³) for the range of nanoparticle sizes described here (0.5 to 450 nm). The time required to settle 1 m in the shallow brine ($\rho_f = 1.1$ g/cm³) ranges from 65 days (for a 450 nm nanoparticles) to 1.45×10^5 years (for a 0.5 nm nanoparticles) (Table S6); likewise in the deep brine layer ($\rho_f = 1.16$ g/cm³) the greater density will require larger time (Table S6). For denser nanoparticles; e.g., pyrite (FeS₂) ($\rho_s = 5$ g/cm³), the settling time in the deep brine layer will require 33 days for 450 nm nanoparticles and 7.31×10^4 years for a 0.5 nm nanoparticle.

These results suggest that the downward transport between the layers may be one cause to explain similarities in size distribution and elemental composition for the larger particles (> 450 nm) between the two layers. However, for nanoparticle sizes < 50 nm (> 14 years required to settle 1 m), downward transport cannot explain the similarities in size distribution and elemental composition between the two layers. Furthermore, the Great Salt Lake is rarely quiescent for periods of one, let alone two months of time. Disturbance of the lake surface due to storms and wind events occurs frequently, potentially mixing material between the two layers.

References

Appelo, C.A.J., and Postma, D. (2005) *Geochemistry, groundwater and pollution*. 2nd Edition. A.A. Balkema Publishers, New York, pp. 123-132; 247-363; 436.

Bolea, E., Gorriz, M.P., Bouby, M., Laborda, F., Castillo, J.R., Geckeis, H. (2006) Multielement characterization of metal-humic substances complexation by size exclusion chromatography, asymmetrical flow field-flow fractionation, ultrafiltration and inductively coupled plasma-mass spectrometry detection: A comparative approach. *Journal of Chromatography A*, **1129**, 236–246.

Christian, P., Von der Kammer, F., Baalousha, M., Hofmann, Th. (2008) Nanoparticles: structure, properties, preparation and behaviour in environmental media. *Ecotoxicology*, **17**, 326–343.

Drever, J.I. (2002) *The Geochemistry of natural waters, surface and groundwater environments*, 3rd ed. reprinted; Prentice Hall: Upper Saddle River, pp. 26-33; 113-119, 185-196.

Fengxiang, H. and Banin, A. (1997) Long-term transformations and redistribution of potentially toxic heavy metals in arid-zone soils incubated: I. Under saturated conditions. *Water, Air, & Soil Pollution* **95**, 399-423.

Litzén, A. (1993) Separation speed, retention, and dispersion in asymmetrical flow field-flow fractionation as functions of channel dimensions and flow rates, *Analytical Chemistry*, **65**, 461-470.

Parkhurst, D.L. and Appelo, C.A.J. (1999) User's guide to PHREEQC (version 2) A computer program for speciation, batch-reaction, one-dimensional transport, and inverse geochemical calculations, USGS.
http://wwwbrr.cr.usgs.gov/projects/GWC_coupled/phreeqc/html/final.html

Prestel, H.; Schott, L.; Niessner, R.; Panne, U. (2005) Characterization of sewage plant hydrocolloids using asymmetrical flow field-flow fractionation and ICP-mass spectrometry. *Water Res.* **39**, 3541-3552.

Ratanathanawongs-Williams, S.K. and Giddings, J.C. (2000) Sample recovery. IN *Field flow fractionation handbook*. (eds. M.E. Schimpf, , K. Caldwell, and J.C. Giddings), Wiley-Interscience, Inc., New York, pp. 325 - 343.

Tables and Figures

Table S1. CC-ICP-MS operation conditions.

OPERATION CONDITIONS	
RF power (W)	1550
Plasma gas flowrate (L/min)	15
Hydrogen flowrate (mL/min)	2.5
Helium flowrate (mL/min)	2.5
Carrier flowrate (L/min)	0.8
Make-up gas (L/min)	0.2
Auxiliary gas (L/min)	0.9
Sample flowrate (mL/min)	0.3
Acquisition time per isotope (sec)	0.05
Repetition	3
Total acquisition time for 19 isotopes (sec)	2.85
Total running time (sec)	1500 - 1860
Tuning solution: ¹³³ Cs mean (cps) wth H ₂ in collision cell % RSD	34,000 < 3%
Sample nebulizer tubing: Material Internal diameter (mm)	Tygon 1.02
AF4 carrier tubing: Material Internal diameter (mm)	Peek 0.25

Table S2. Great Salt Lake synthetic solution composition.

Salt	Concentration (mol/g_{solution})	Concentration (g/L)	Grams in 100mL milli-Q water	Salt Purity	Salt brand
NaCl	1.99E-03	116.7884	11.6788	99.999%	Sigma- Aldrich
MgCl ₂	1.46E-04	13.9657	1.3966	99.99%	Sigma
MgSO ₄	3.73E-05	4.4874	0.4487	99.99+%	Aldrich
K ₂ SO ₄	3.21E-05	5.5877	0.5588	99.99%	Aldrich
CaSO ₄	4.88E-06	0.6306	0.0631	99.99+%	Aldrich

Table S3. Average concentrations of multielement analysis in FA (filter acidified) and RA (raw acidified) GSL water samples, shallow and deep brines.

Element	Units	Mean FA Shallow	Mean RA Shallow	Mean FA Deep	Mean RA Deep
Na	mg/L	43748.10	44539.20	55920.38	56787.75
Mg	mg/L	4506.30	4585.77	5857.31	5927.74
S	mg/L	3304.71	3325.41	4255.99	4207.50
Cl	mg/L	83878.20	83917.80	106984.13	105842.25
K	mg/L	2543.76	2576.07	3275.10	3309.98
Ca	mg/L	268.42	272.88	293.48	299.89
Al	µg/L	26.76	82.73	52.66	1960.98
Mn	µg/L	11.51	14.77	54.59	105.10
Fe	µg/L	9.57	60.86	26.46	1675.98
Si	µg/L	10381.67	11145.06	10277.00	19026.50
Co	µg/L	< 0.4	0.40	0.47	0.73
Ni	µg/L	< 3.0	< 3.0	< 0.3	3.04
Cu	µg/L	4.34	5.22	1.65	17.12
Zn	µg/L	< 20.0	< 20.0	< 20	30.23
As	µg/L	138.59	139.47	180.80	188.08
Mo	µg/L	51.90	51.71	23.77	45.35
Sb	µg/L	13.71	13.72	12.48	13.25
Ba	µg/L	141.31	143.33	129.87	159.14
Pb	µg/L	0.51	0.54	< 0.3	5.80
U	µg/L	9.50	9.44	7.25	7.87
Se	µg/L	0.52	0.65	0.46	0.65

Table S4. PHREEQC model for GSL shallow brine using RA water samples. *SI* accounts for saturation index. It is presented only the positive *SI* values obtained.

Conditions:	
pH	8.3
density (g/mL)	1.1
temperature (°C)	2-30
pe	3.4

	Temperature:	2°C		Temperature:	30°C	
	<i>Phase</i>	<i>SI</i>		<i>Phase</i>	<i>SI</i>	
1	Ba3(AsO4)2	7.95	Ba3(AsO4)2	Ba3(AsO4)2	6.81	Ba3(AsO4)2
2	Barite	1.43	BaSO4	Barite	0.94	BaSO4
3	Boehmite	0.74	AlOOH	Boehmite	0.03	AlOOH
4	CaMoO4	0.48	CaMoO4	CaMoO4	0.54	CaMoO4
5	Chalcedony	0.49	SiO2	Chalcedony	0.11	SiO2
6	Chrysotile	7.04	Mg3Si2O5(OH)4	Chrysotile	10.46	Mg3Si2O5(OH)4
7	CoFe2O4	12.97	CoFe2O4	CoFe2O4	20.85	CoFe2O4
8	Cristobalite	0.29	SiO2	Cupricferrite	9.24	CuFe2O4
9	Cupricferrite	0.86	CuFe2O4	Cuprousferrite	8.72	CuFeO2
10	Cuprousferrite	5.86	CuFeO2	Diaspore	1.7	AlOOH
11	Diaspore	2.66	AlOOH	Fe(OH)2.7Cl.3	6.63	Fe(OH)2.7Cl.3
12	Fe(OH)2.7Cl.3	4.01	Fe(OH)2.7Cl.3	Ferrihydrite	2.92	Fe(OH)3
13	Gibbsite	1.31	Al(OH)3	Gibbsite	0.22	Al(OH)3
14	Goethite	1.94	FeOOH	Goethite	5.62	FeOOH
15	Halloysite	3.1	Al2Si2O5(OH)4	Halloysite	0.69	Al2Si2O5(OH)4
16	Hematite	6.21	Fe2O3	Hematite	13.71	Fe2O3
17	Hercynite	1.94	FeAl2O4	Hercynite	1.39	FeAl2O4
18	Kaolinite	5.73	Al2Si2O5(OH)4	K-Jarosite	0.01	KFe3(SO4)2(OH)6
19	Maghemite	0.29	Fe2O3	Kaolinite	2.73	Al2Si2O5(OH)4
20	Magnesioferrite	2.03	Fe2MgO4	Lepidocrocite	4.57	FeOOH
21	Magnetite	7.53	Fe3O4	Maghemite	5.53	Fe2O3
22	Quartz	0.97	SiO2	Magnesioferrite	12.18	Fe2MgO4
23	Sepiolite	4.97	Mg2Si3O7.5OH:3H2O	Magnetite	15.92	Fe3O4
24	Sepiolite(A)	3.62	Mg2Si3O7.5OH:3H2O	Quartz	0.55	SiO2
25	U3O8	13.86	U3O8	Sepiolite	6.91	Mg2Si3O7.5OH:3H2O
26	U4O9	13.91	U4O9	Sepiolite(A)	3.56	Mg2Si3O7.5OH:3H2O
27	Uraninite	1.98	UO2			

Table S5. PHREEQC model for GSL deep brine using RA water samples. *SI* accounts for saturation index. It is presented only the positive *SI* values obtained.

Conditions:							
pH	7.7						
density (g/mL)	1.16						
temperature (°C)	13- 20						
pe	-5						
	Temperature:	13°C		Temperature:	20°C		
	<i>Phase</i>	<i>SI</i>		<i>Phase</i>	<i>SI</i>		
1	Al(OH)3(am)	0.3	Al(OH)3	Al(OH)3(am)	0.1	Al(OH)3	
2	Al2O3	2.45	Al2O3	Al2O3	2.21	Al2O3	
3	Anilite	3.15	Cu0.25Cu1.5S	Anilite	2.71	Cu0.25Cu1.5S	
4	BlaubleiI	1.21	Cu0.9Cu0.2S	BlaubleiI	1.29	Cu0.9Cu0.2S	
5	BlaubleiII	1.04	Cu0.6Cu0.8S	BlaubleiII	1.25	Cu0.6Cu0.8S	
6	Boehmite	2.53	AlOOH	Boehmite	2.36	AlOOH	
7	CaMoO4	1.68	CaMoO4	CaMoO4	1.76	CaMoO4	
8	Chalcedony	0.79	SiO2	Chalcedony	0.7	SiO2	
9	Chalcocite	3.35	Cu2S	Chalcocite	3.09	Cu2S	
10	Chalcopyrite	10.08	CuFeS2	Chalcopyrite	9.26	CuFeS2	
11	Chrysotile	8.17	Mg3Si2O5(OH)4	Chrysotile	9.06	Mg3Si2O5(OH)4	
12	Clausthalite	10.57	PbSe	Clausthalite	9.96	PbSe	
13	CoS(alpha)	0.18	CoS	CoS(beta)	3.61	CoS	
14	CoS(beta)	3.81	CoS	CoSe	3.53	CoSe	
15	CoSe	3.58	CoSe	Covellite	0.76	CuS	
16	Covellite	1.16	CuS	Cristobalite	0.5	SiO2	
17	Cristobalite	0.59	SiO2	Cu2Se(alpha)	8.89	Cu2Se	
18	Cu2Se(alpha)	9.21	Cu2Se	CuSe	6.43	CuSe	
19	Cu3Se2	0.61	Cu3Se2	Diaspore	4.11	AlOOH	
20	Diaspore	4.35	AlOOH	Djurleite	2.88	Cu0.066Cu1.868S	
21	Djurleite	3.31	Cu0.066Cu1.868S	FeSe	1.17	FeSe	
22	FeSe	1.23	FeSe	Galena	1.93	PbS	
23	Galena	2.51	PbS	Gibbsite	2.66	Al(OH)3	
24	Gibbsite	2.93	Al(OH)3	Halite	0	NaCl	
25	Halite	0.01	NaCl	Halloysite	6.58	Al2Si2O5(OH)4	
26	Halloysite	7.17	Al2Si2O5(OH)4	Hercynite	5.63	FeAl2O4	
27	Hercynite	5.68	FeAl2O4	Kaolinite	8.82	Al2Si2O5(OH)4	
28	Kaolinite	9.56	Al2Si2O5(OH)4	MoS2	22.59	MoS2	
29	MoS2	24.54	MoS2	NiS(alpha)	0.26	NiS	
30	NiS(alpha)	0.44	NiS	NiS(beta)	5.76	NiS	
31	NiS(beta)	5.94	NiS	NiS(gamma)	7.46	NiS	
32	NiS(gamma)	7.64	NiS	NiSe	7.15	NiSe	
33	NiSe	7.18	NiSe	Orpiment	16.67	As2S3	
34	Orpiment	18.72	As2S3	Pyrite	7.93	FeS2	
35	Pyrite	8.5	FeS2	Quartz	1.16	SiO2	
36	Quartz	1.26	SiO2	Realgar	0.46	AsS	
37	Realgar	1.2	AsS	Sepiolite	6.82	Mg2Si3O7.5OH:3H2O	
38	Sepiolite	6.31	Mg2Si3O7.5OH:3H2O	Sepiolite(A)	4.14	Mg2Si3O7.5OH:3H2O	
39	Sepiolite(A)	4.13	Mg2Si3O7.5OH:3H2O	Sphalerite	1.38	ZnS	
40	Sphalerite	1.36	ZnS	Spinel	0.55	MgAl2O4	
41	Spinel	0.22	MgAl2O4	Uraninite	2.06	UO2	
42	Uraninite	2.23	UO2				

Table S6. Settling velocities and settling times for representative compounds and different nanoparticles sizes.

Representative compound	Particle diameter (nm)	Particle density (g/cm ³)	Fluid density (g/cm ³)	Settling velocity (cm/s)	Settling time (d)	Settling time (yr)
Boehmite	1000	3.0	1.1	8.7E-05	13.2	0.036
	450			1.8E-05	65.4	0.18
	250			5.5E-06	211.9	0.6
	50			2.2E-07	5298.3	14.5
	10			8.7E-09	132456.5	362.9
	1			8.7E-11	13245653.7	36289.5
	0.5			2.2E-11	52982614.7	145157.8
Boehmite	1000	3.0	1.16	8.47E-05	13.7	0.037
	450			1.71E-05	67.5	0.18
	250			5.29E-06	218.7	0.6
	50			2.12E-07	5467.4	15.0
	10			8.47E-09	136683.9	374.5
	1			8.47E-11	13668387.3	37447.6
	0.5			2.12E-11	55220284.7	151288.5
Pyrite	1000	5.0	1.16	1.73E-04	6.7	0.018
	450			3.51E-05	33.0	0.090
	250			1.08E-05	106.8	0.3
	50			4.34E-07	2669.8	7.3
	10			1.73E-08	66744.3	182.9
	1			1.73E-10	6674433.3	18286.1
	0.5			4.34E-11	26697733.1	73144.5

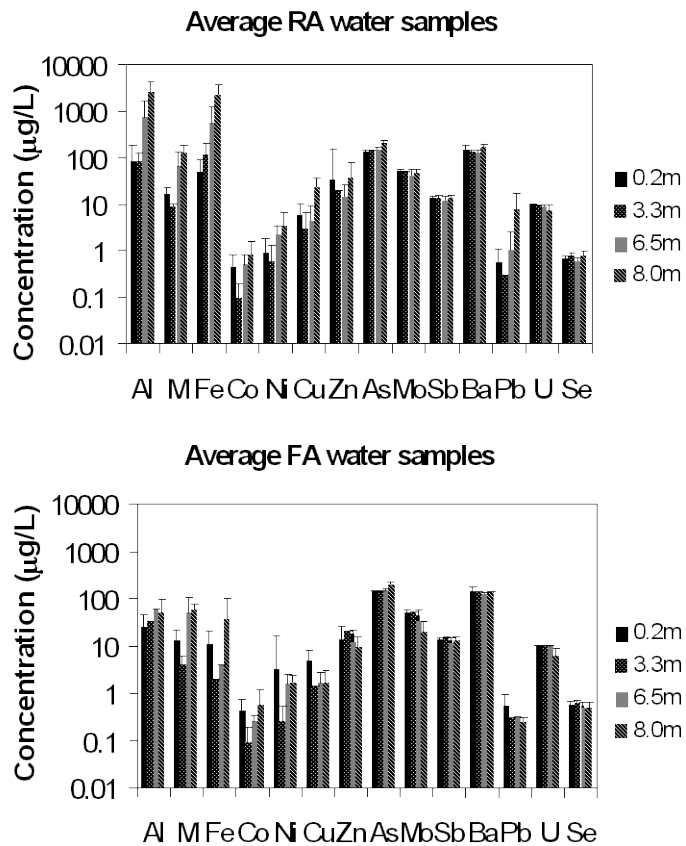
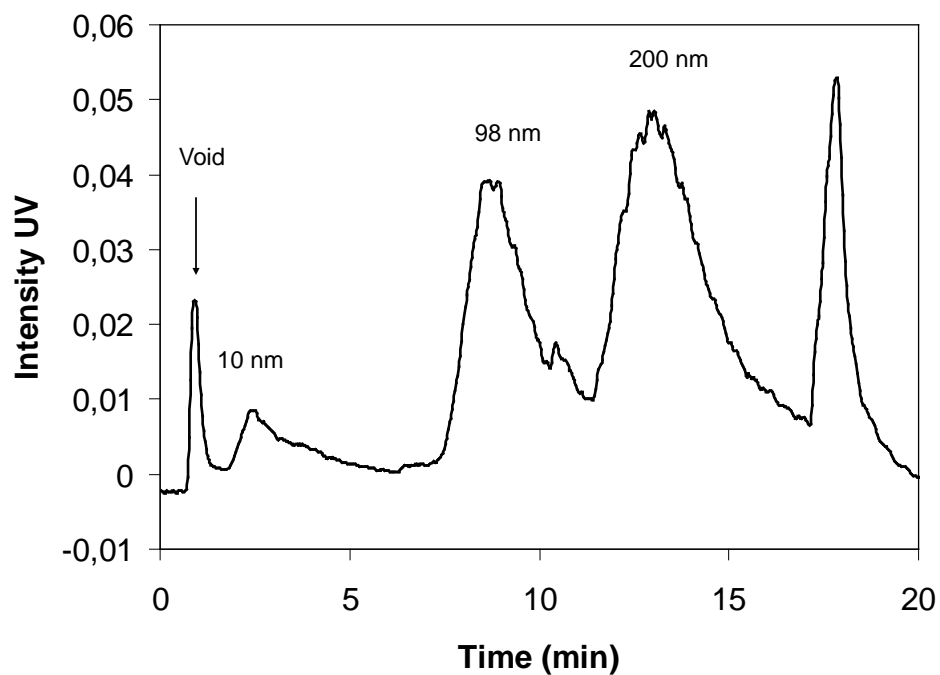


Figure S1. Average total concentrations of trace metals in raw acidified samples (RA) and filtered acidified samples (FA) taken at four stations (2267, 2767, 2565 and 3510) and different depths (0.2, 3.0, 6.5 and 8.0 m). RA represents dissolved + particulate concentrations; whereas FA represents dissolved concentrations.

Fractogram for carboxylated PS (98 & 200nm) and gold colloid (10 nm) nanoparticles



Calibration curve for nanoparticles

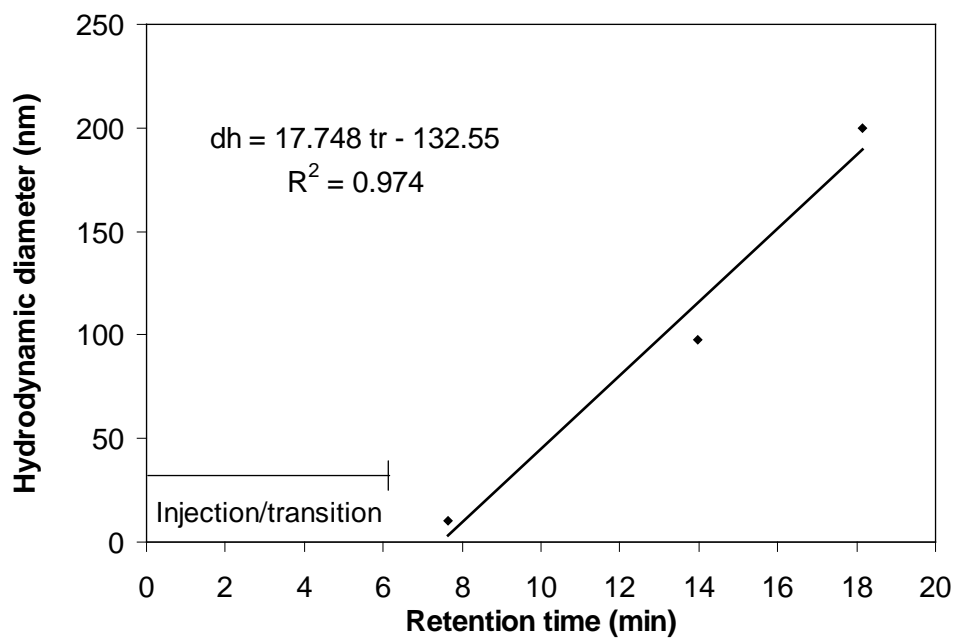
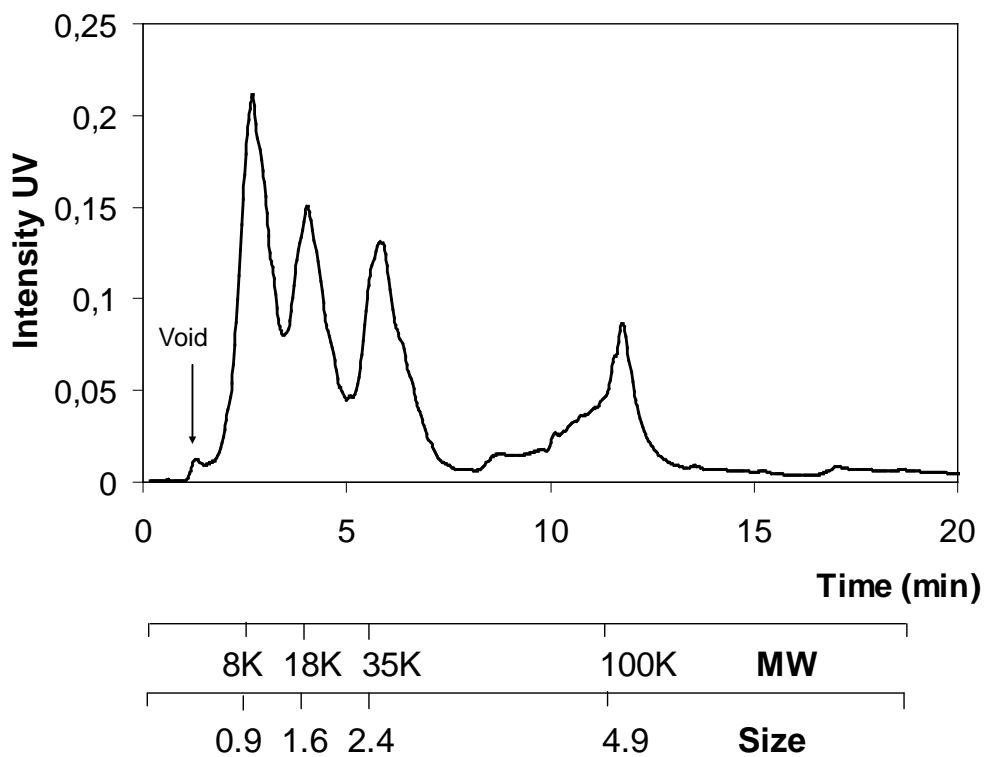


Figure S2. Calibration curve for latex beads and colloidal gold nanoparticles for a size range of 10 to 250 nm.

Fractogram using Polystyrene Sulfonate Standards (PSS)



Calibration curve for macromolecules

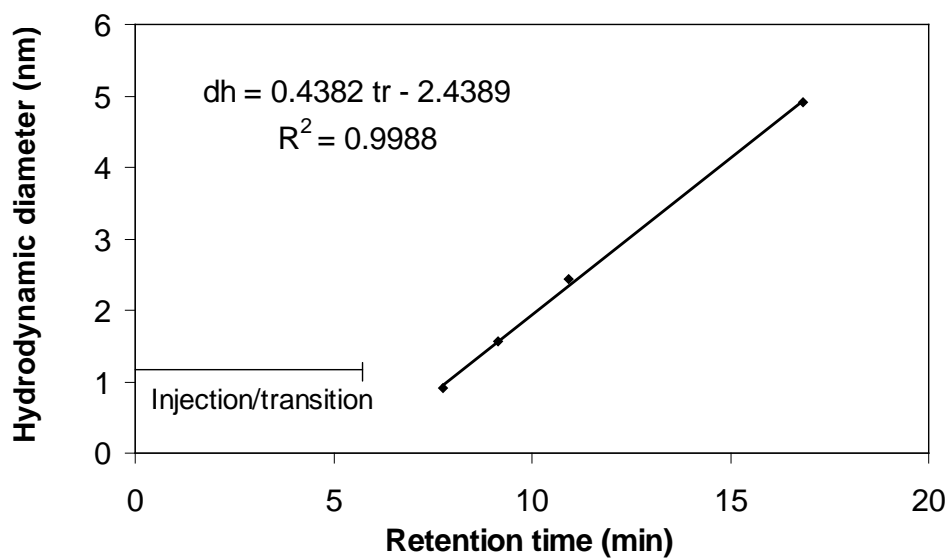


Figure S3. Calibration curve for polystyrene sulfonates standards (PSS) for a size range of 0.9 to 5 nm

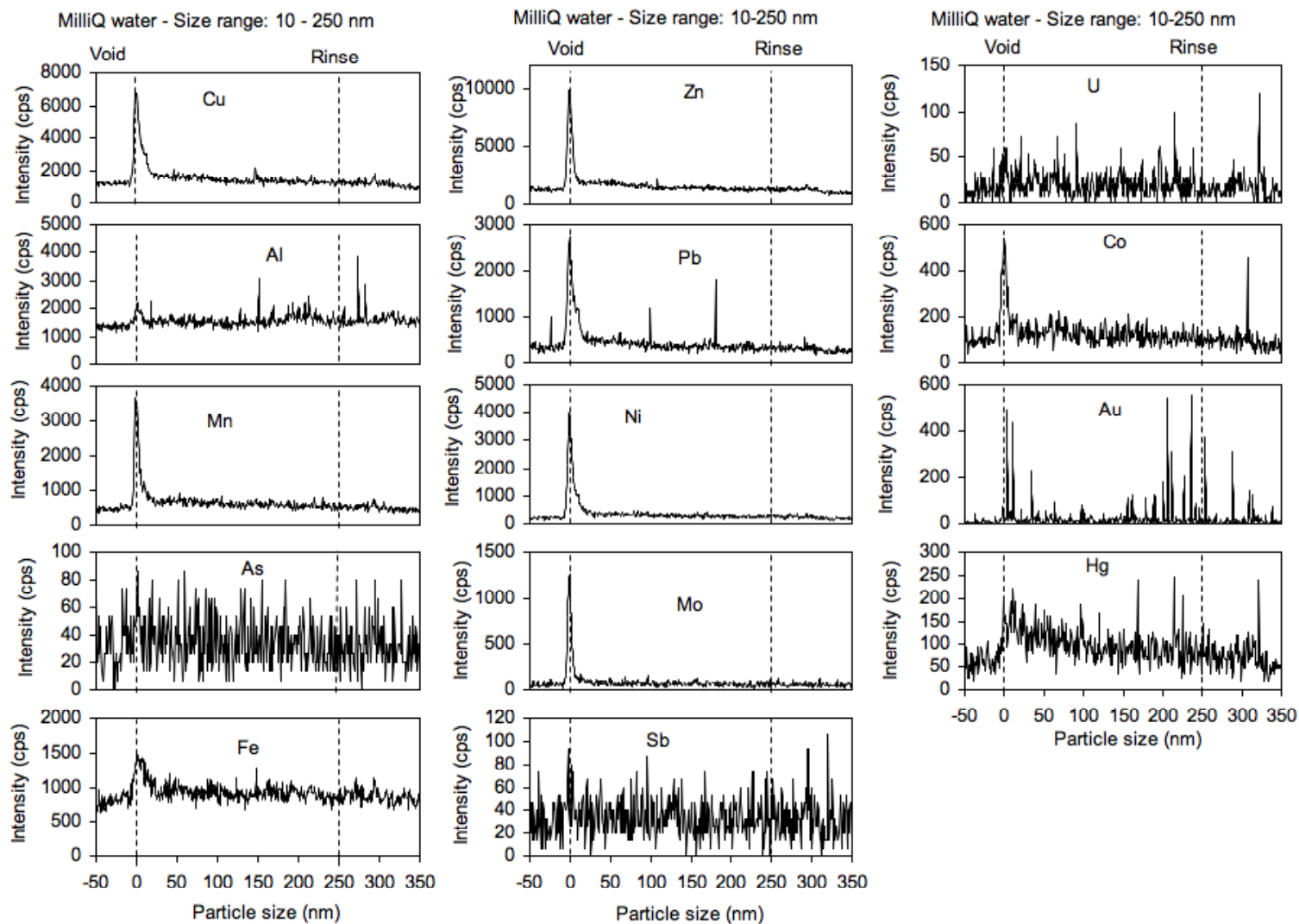


Figure S4a. Fractograms of the milli-Q water for size range: 10 – 250 nm.

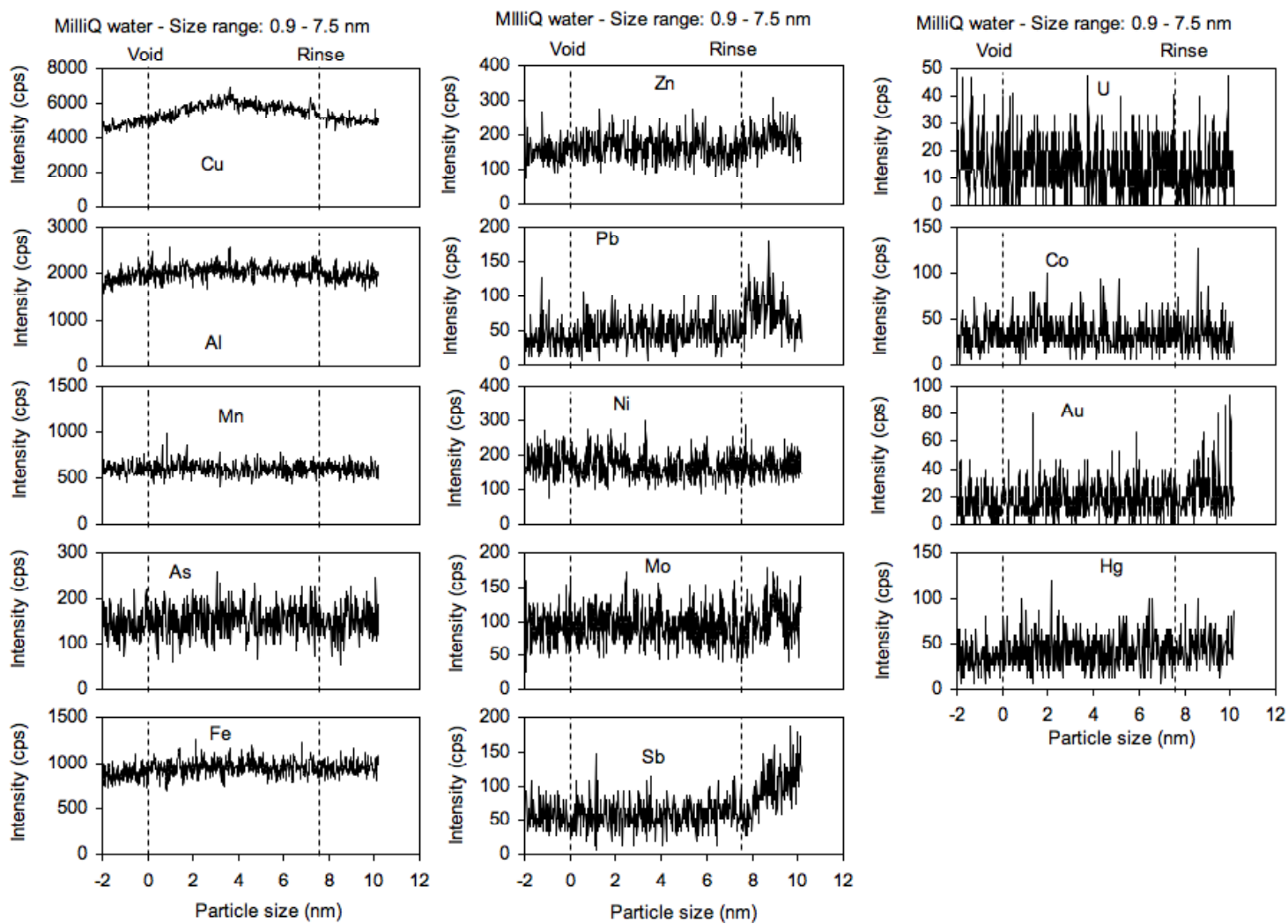


Figure S5a. Fractograms of the milli-Q water for size range: 0.9 – 7.5 nm.

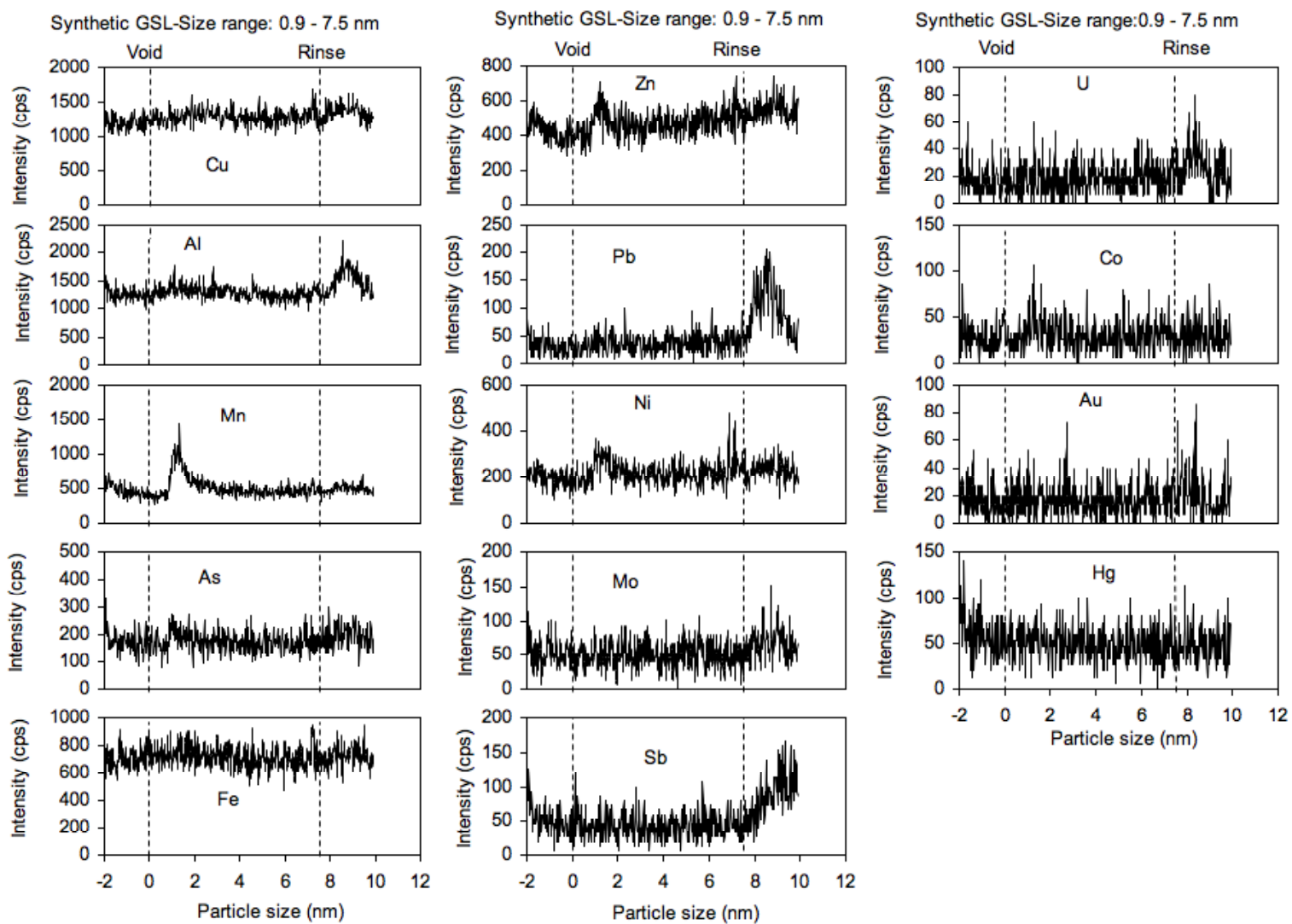
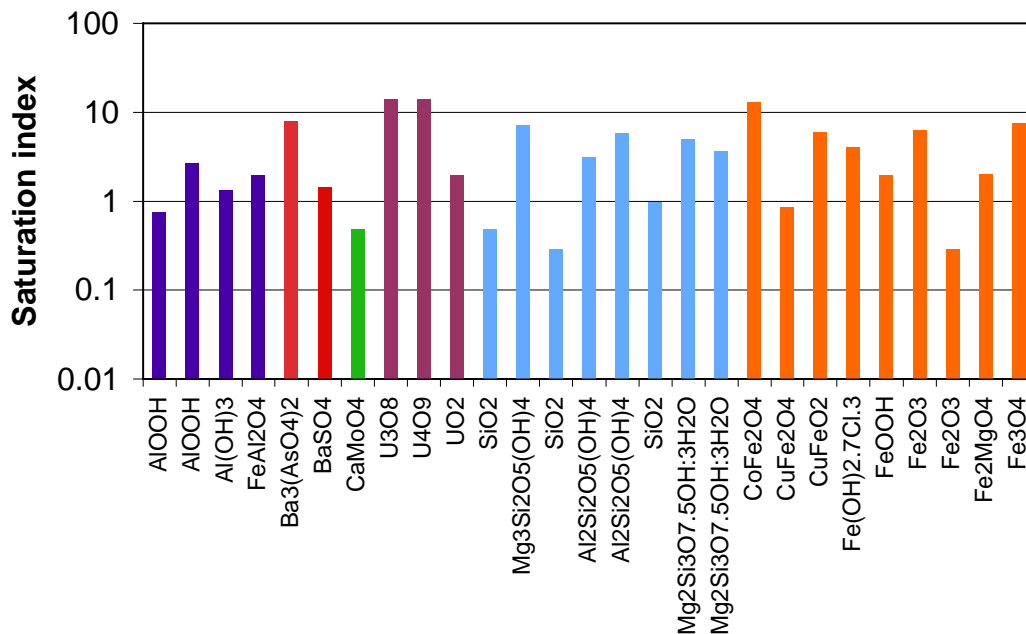


Figure S5b. Fractograms of the GSL synthetic for size range: 0.9 – 7.5 nm.

Predicted phases using GSL shallow brines



Predicted phases using GSL deep brines

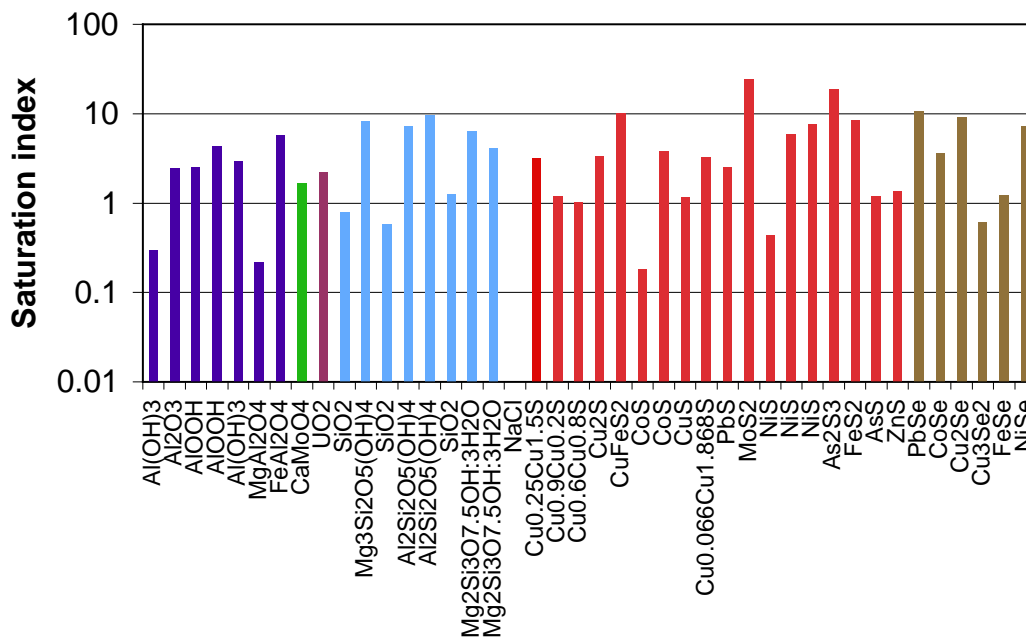


Figure S6. Predicted precipitate phase using USGS PHREEQC software. Top: shallow brine. Bottom: deep brine.

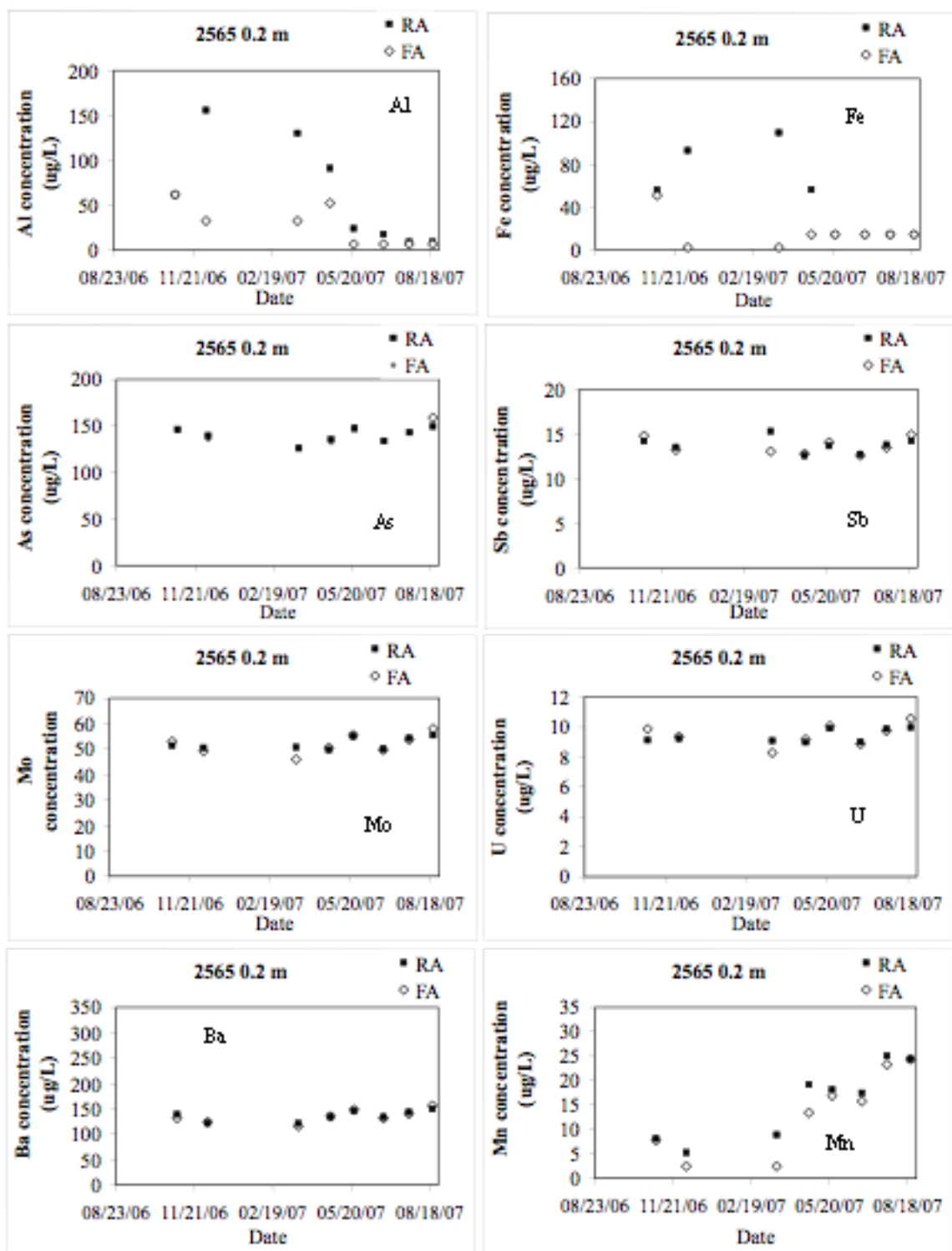


Figure S7. Trace metals trajectories for the shallow brines represented by site 2565 at 0.2 m.

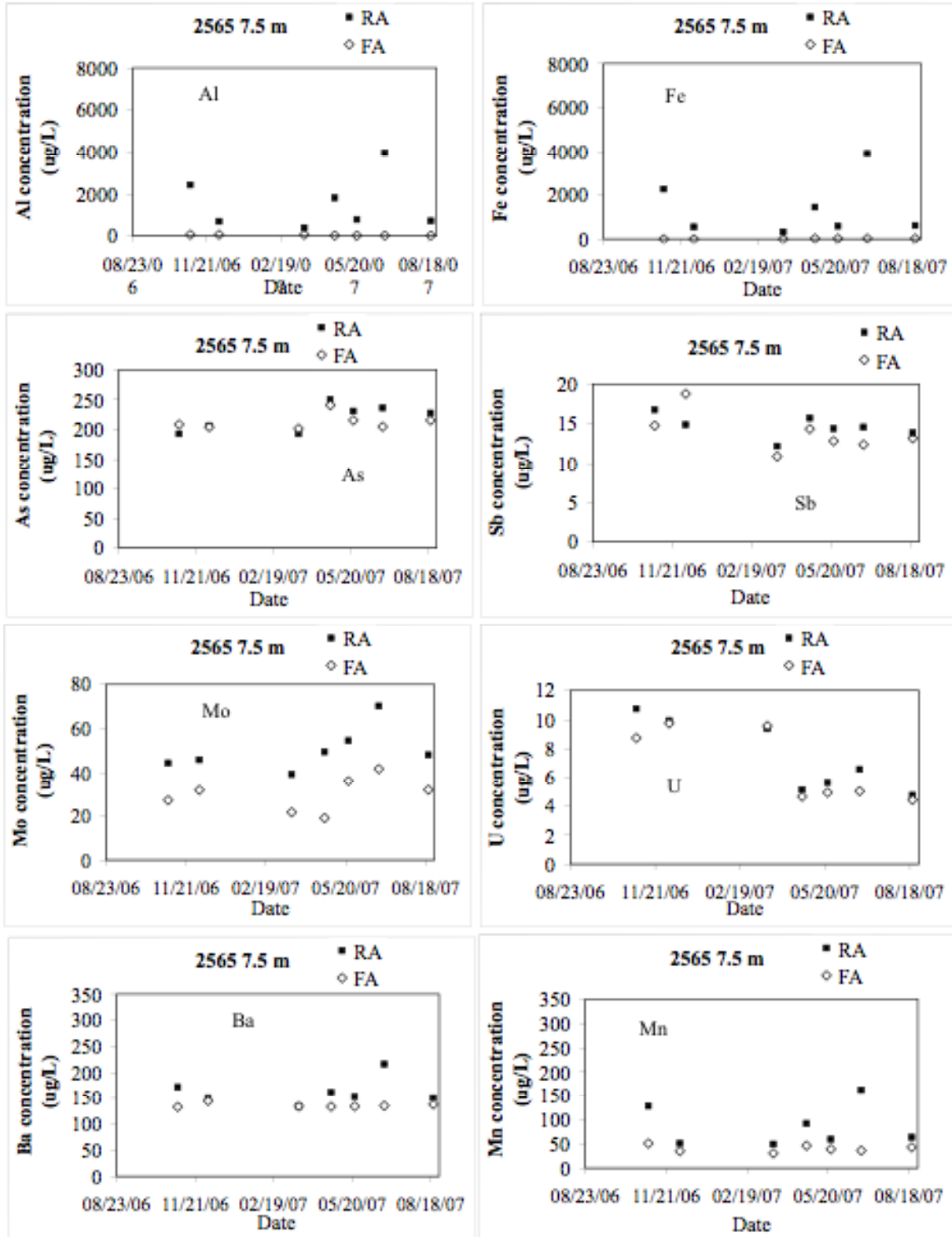


Figure S8. Trace metals trajectories for deep brines represented by site 2565 at 7.5 m